Lamination and mixing in three fundamental flow sequences driven by electromagnetic body forces

L. Rossi, D. Doorly, and D. Kustrin
Department of Aeronautics, Imperial College London, London SW7 2AZ, United Kingdom
(Received 19 June 2011; revised manuscript received 16 February 2012; published 22 August 2012)

This article pursues the idea that the degree of striations, called lamination, could be engineered to complement stretching and to design new sequential mixers. It explores lamination and mixing in three new mixing sequences experimentally driven by electromagnetic body forces. To generate these three mixing sequences, Lorentz body forces are dynamically controlled to vary the flow geometry produced by a pair of local jets. The first two sequences are inspired from the "tendril and whorl" and "blinking vortex" flows. The third novel sequence is called the "cat's eyes flip." These three mixing sequences exponentially stretch and laminate material lines representing the interface between two domains to be mixed. Moreover, the mixing coefficient (defined as $1-\sigma^2/\sigma_0^2$ where σ^2/σ_0^2 is the rescaled variance) and its rate grow exponentially before saturation. This saturation of the mixing process is related to the departure of the mixing rate from an exponential growth when the striations' thicknesses reach the diffusive length scale of the measurements or species and dyes. Incidentally, in our experiments, for the same energy or forcing input, the cat's eyes flip sequence has higher lamination, stretching, and mixing rates than the tendril and whorl and the blinking vortex sequences. These features show that bakerlike *in situ* mixers can be conceived by dynamically controlling a pair of local jets and by integrating lamination during stirring stages with persistent geometries. Combined with novel insights provided by the quantification of the lamination, this paper should offer perspectives for the development of new sequential mixers, possibly on all scales.

DOI: 10.1103/PhysRevE.86.026313 PACS number(s): 47.51.+a, 47.15.−x, 47.65.−d, 47.85.L−

I. INTRODUCTION

Mixing processes are important for industrial, biological, physical, and environmental flows. For example, mixing impacts on chemistry [1,2], biological processes, and clinical diagnostics [3–5], geophysical systems [6–8], plasma systems [9,10], and astrophysical flows [11,12]. When the scale and Reynolds number are reduced, the flows are laminar and cannot be mixed using turbulence [13]. Consequently, new flows need to be engineered [14]. In an attempt to reproduce turbulent mixing in laminar flows, turbulentlike multiscale flows have recently been discussed in literature [15,16]. An older approach to enhance mixing in low Reynolds number flows is to use chaotic advection and bakerlike processes to achieve mixing [17–20]. Indeed, since 1893 and the seminal talk of Reynolds [21], it is well known that, like a baker making pastry, a proper combination of stretching and folding within flows is amenable to generate an exponential growth of material interfaces. It can be noted that numerous flows, producing chaotic trajectories, have been studied in literature, e.g., Refs. [22–35].

Lamination is the ensemble of mechanisms generating striations within flows. It includes folding, rolling, bending, line encounters, foliation [36], etc. Combined with shear and/or strain, lamination is key for producing exponential growths of interfaces in complex flows [37]. Moreover, lamination enhances mixing when the thicknesses of the striations are reduced. In a diffusive mixture, this enhancement is at the heart of the merging of filaments [38] and the building of mixing as aggregation and self-convolution processes [39–41]. To date, despite being of importance for mixing processes [42], the lamination of complex flows is still partially explored [43–45] and is often considered as a subproduct of stretching. Recently, a process and a new measure have been proposed to explore lamination [37,46]. The lamination process identifies a lamination rate based on the spatial variation in the Lagrangian angular velocity extracted using spatial measurements of the Lagrangian acceleration [37,47]. The measure of lamination compares the total length [area in three dimensions (3D)] of an interface within a disk (sphere in 3D) centered on the interface to the disk's diameter (main section in 3D) and is used in Ref. [46] to show good agreement between the lamination rate and the lamination measured for single- and multiscale flows.

This article pursues the idea that lamination can be engineered [37,46,48,49] to design new mixers with tailored properties. A study of stirred interfaces (without molecular diffusion) is performed with direct measurements of their stretching and the distribution of their striations' thicknesses. It can be noted that the striations' thicknesses of the stirred interfaces are the distance over which the diffusion would need to act to finalize the mixing of diffusive dyes or species. In the present paper, these thicknesses are locally extracted using the new lamination measurement proposed in Ref. [46]. We prefer this direct investigation rather than using Lyapunov exponents to estimate these quantities [45]. Indeed, the use of Lyapunov exponents to characterize the properties of nonuniform mixing processes (e.g., the presence of islands) may lead to approximations. Moreover, if due to the flow's incompressibility, local Lyapunov exponents can be related to the decrease in striations' thicknesses, it is not obvious that such a method can predict the long run multiplication of layers in complex flows. For example, such exponential trends cannot predict the generation of striations due to the rolling of interfaces within persisting eddies [37,43].

Lamination, stretching, and mixing are explored in three new sequences of flows before discussing the interweaving between the lamination and the saturation of the mixing rate. These sequences result from the combination of mixing "building blocks" using the temporal persistence of different flow geometries. The first two sequences are inspired from milestone flows proposed to produce mixing by chaotic

advection, the "blinking vortex" (BV) and the "tendril and whorl" (TW) [17,22]. The third novel sequence relies on the flipping of a cat's eyes flow and is named "cat's eyes flip" (CF).

To generate these mixing sequences, the authors dynamically control the position of a pair of jets driven by electromagnetic forces. The experimental apparatus is similar to the ones described in Refs. [50,51]. One novelty comes from a three-axis mechanical device controlling the position of the magnets in space and time. It is worth mentioning that, within the past 30 years, the study of mixing and time-dependent two-dimensional (2D) chaotic advection have led to the conception of different experimental setups, which are not driven by electromagnetic forces, e.g., rotating cylinders [52], baffled cavity flow [53], moving rods [54–56], flow suction and injection [24], oscillatory convection in binary mixtures [57], time-dependant Rayleigh-Bénard convection [23], and rotating devices with flow inlets and outlets [58,59].

II. FLOWS DRIVEN BY ELECTROMAGNETIC FORCES

A. Experimental setup

Tailored flows are produced within a shallow layer of brine using electromagnetic forces. The experimental apparatus used to generate these flows driven by body forces is described in Fig. 1. The use of body forces presents the advantage of adding a source of momentum within the flow, and the shallow layer permits working with quasi-two-dimensional flows [50,51,60].

The experiments are performed in brine made of a mixture of water and 60 g/l of sodium sulfate Na_2SO_4. The horizontal size of the rig is about 800 mm × 600 mm, and the thickness of the shallow layer is about $H = 4.3$ mm. The vertical height of the water on the side of the tank is about 300 mm. The brine is left at rest to produce a stable stratification. Conductivity measurements are performed to check the properties of the upper layer of the brine, i.e., within the mixing domain. The measured conductivity is about $\sigma = 3.5$ S/m. The average concentration within the upper layer is then estimated to be about 40 g/l of Na_2SO_4 [61,62]. The corresponding viscosity

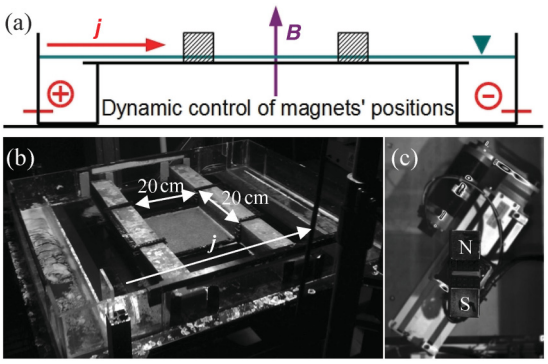

FIG. 1. (Color online) (a) Schematic and (b) photograph of the experimental rig. (c) The three-axis robot and the pair of permanent magnets (North and South) are illustrated in the photograph. The arrows labeled $\boldsymbol{j}$ indicate the direction of the electrical current crossing the brine. The arrow labeled $\boldsymbol{B}$ indicates the direction of the magnetic field (produced by the permanent magnets placed underneath the wall) contributing to the generation of horizontal body forces.

is $\nu = 1.126 \times 10^{-6} \mathrm{m}^2/\mathrm{s}$ for a density of $\rho = 1.0343 \mathrm{kg/m}^3$. Moreover, the flow domain is reduced to 200 × 200 mm^2 to study mixing in a bounded domain. As illustrated in Fig. 1, this is achieved using plastic (LEGO) walls on two sides and foam on the other sides.

The electromagnetic body forces are generated by the combination of a pair of square permanent magnets (denoted as N and S in Fig. 1) producing a magnetic field $\boldsymbol{B}$ and an electrical current $\boldsymbol{j}$ crossing the brine. The permanent magnets are two cubes of $L_M = 40$ mm sides. Their measured intensity is $B_r = 1.2T$. They are placed on a 2 cm thick iron plate, and their upper surface is at 6.1 mm from the brine. As indicated in Fig. 1, the magnets are placed underneath the wall supporting the brine, and the main component of the magnetic field contributing to the electromagnetic forcing ($\boldsymbol{j} \times \boldsymbol{B}$) is perpendicular to the wall. The alternated configuration of the pair of magnets, i.e., with North and South poles, permits the generation of opposite forces above each magnet. The electrical current crossing the brine is imposed by two sets of platinum electrodes placed on each side of the experimental rig. The electrical current intensity is $I = 30$ mA, which leads to a current density of $j = 11.6 \mathrm{A/m}^2$ within the shallow layer. The direction of the electrical current is indicated by the arrows labeled $\boldsymbol{j}$ in Fig. 1. It can be noticed that the electrical power consumed by these experiments is about 0.13 W.

The dynamic control of the magnets' positions is one novelty since [50]. This is achieved using a three-axis mechanical device driven by three servomotors with independent controllers. Figure 1(c)) gives a top view photograph of the magnets' pair mounted on the mechanical device with alternated polarity. The position and orientation of the magnets' distribution can be varied in time. A centered rotation of the pair of magnets permits controlling the main geometry of the flow. A two-dimensional translation of the pair of magnets allows varying the spatial position of these geometries. This translation is achieved using one rotation and one translation (similar to cylindrical coordinates) in addition to the centered rotation. For the three sequences, the magnets cyclically move in 1.8 s between two positions where they stay steady for a time. This time is chosen longer than the viscous diffusion's time, i.e., $H^2/\nu \sim 16$ s so as to establish quasisteady flows during the steady stages.

The cat's eyes flip and the tendril and whorl sequences are performed with a rotation of the pair of magnets, which is centered within the flow domain. The orientation 0° is defined as the configuration with the pair of magnets orthogonal to the electrical current. With this reference, the steady positions of the cat's eyes flip are oriented at $-15°$ and $+15°$. The steady positions of the tendril and whorl are oriented at 0° and 90°. The blinking vortex sequence is a translation of the pair of magnets oriented at 90°. The translation is along the median axis in the direction of the electrical current. The two steady positions are at $\pm 0.5 L_M$ where the origin is the center of the mixer. Figure 2 illustrates these displacements. Except, if stated differently, the pair of magnets stays steady for 22 s, and the period of the forcing cycle is $T_{\mathrm{cyc}} = 47.6$ s for the three sequences.

It can be noted that annular electromagnetic rigs, allowing the oscillation of an array of magnets [63,64] and/or its continuous displacement [65], can be found in literature.

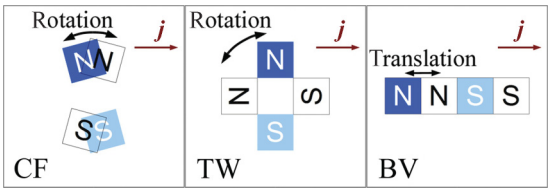

FIG. 2. (Color online) Schematic of the displacements of the pair of North and South magnets (denoted as N and S) for the three mixing sequences. The cat's eyes flip, the tendril and whorl, and the blinking vortex sequences are denoted as CF, TW, and BV, respectively. The arrows labeled $\boldsymbol{j}$ indicate the direction of the electrical current.

Continuous recordings of the flows are performed, during more than 20 min, at 6 Hz with a 2048 × 2048 pixel^2 14 bit camera using a LaVision acquisition system. A particle image velocimetry (PIV) method is then applied to pairs of consecutive pictures to measure the velocity fields. The in-house PIV code used is an iterative process with a subpixel interpolation to estimate the most likely displacement with a numerical accuracy of 0.05 pixels. The effective accuracy of the most likely displacements measured is 0.2 pixels, which is about 1% of the maximum displacement. It can be noted that the code includes an efficient parallelization of the tasks for multicore computing. For practical guides about PIV techniques, the reader can refer to Refs. [66,67].

The PIV measurements are highly resolved in space with 8.375 pixels per millimeter. The 16 pixels final correlation windows are about 1.9 mm, which is more than 20 times smaller than the size of the magnets. The distance between two points of the PIV grid is 8 pixels. Taking advantage of a 50% overlap, a standard 3 × 3 mobile average smoothing is performed on the validated PIV data. The temporal resolution of the experiments is also high with 285 PIV measurements for each period.

B. Electromagnetic forcing of flow sequences

Body forces have been growingly used to manipulate flows for 15 years [68–77]. These forcing schemes rely on the introduction of a term source $\boldsymbol{f}/\rho$ within the momentum equation,

$$\frac{\partial \boldsymbol{u}}{\partial t} + (\boldsymbol{u}\cdot\boldsymbol{\nabla})\boldsymbol{u} = -\frac{1}{\rho}\boldsymbol{\nabla} P + \nu\,\Delta\boldsymbol{u} + \frac{1}{\rho}\boldsymbol{f}.$$

In the case of the electromagnetic forcing, the term source results from the combination of an electrical current crossing the flow in the presence of a magnetic field producing a Lorentz force $\boldsymbol{f}/\rho = (\boldsymbol{j}\times\boldsymbol{B})/\rho$.

The physical and numerical descriptions of the electromagnetic forces are now mature [60,78,79]. As a consequence, they provide an interesting tool for fundamental studies, and they have been successfully used in numerical simulations [60,71,80].

Figure 3 gives the horizontal distribution of the Lorentz body forces (computed accordingly to Refs. [60,78]) driving the flow for the three sequences (CF, TW, and BV) investigated. The electromagnetic forces are located above the magnets. They are locally pumping the flow in the directions indicated by the superimposed arrows. According to the displacement of the magnets, see Fig. 2, the sequences are produced by the cyclic variations in the electromagnetic forces. These forces vary between two steady positions denoted as A and B in Fig. 3. Varying the relative positions of the local pumping by the electromagnetic forces permits the control of different flow geometries so as to design the mixing sequences.

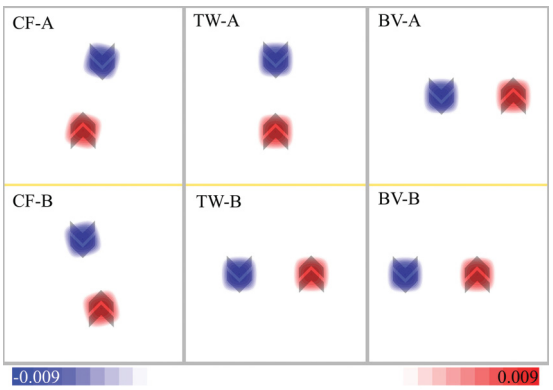

FIG. 3. (Color online) The three columns show the horizontal distribution of the body forcing, normalized by gravity, during the steady stages (denoted as A and B) of the three sequences, from left to right: cat's eyes flip, tendril and whorl, and blinking vortex. The chevrons indicate the directions in which the flow is pumped.

C. Flow sequences

The flow sequences are explored using velocity measurements. The velocity fields are obtained using continuous PIV measurements over the entire mixing domain of size $5L_M \times 5L_M$. The temporal average of the root mean square velocities $\boldsymbol{u}_{\rm rms}$ (computed over space) are given in Table I for CF, TW, and BV sequences. Their mean $\boldsymbol{u}_{\rm ref} = 3.96$ mm/s is taken as the reference velocity. The reference turnover time is then built as $T_{\rm flow} = L_M/\boldsymbol{u}_{\rm ref} = 10.1$ s. With $t^* = t/T_{\rm flow}$, the sequences' dimensionless period is $T^*_{\rm cyc} = 4.7$. The Reynolds number based on the reference velocity and the brine thickness is $\mathrm{Re} = \boldsymbol{u}_{\rm ref} H/\nu \cong 15$. The flows are then laminar. Moreover, the flows being quasi-two-dimensional can be considered as Hamiltonian in the first approximation [17,81].

The typical velocity fields during the steady forcing stages are given in Fig. 4 for the three mixing sequences. The three rows correspond to the different flow sequences (denoted as CF, TW, and BV), and the two columns to the steady configurations which are denoted as A and B. The maxima of the velocities are observed above the magnets, i.e., where the flow is pumped. The typical intensity of these velocity maxima is about three times the root mean square velocity of the flows as illustrated by the distributions of $\|\boldsymbol{u}\|/\boldsymbol{u}_{\rm ref}$. The centers of the elliptical regions are indicated by circles showing the

TABLE I. Temporal average of the root mean square values of velocity $\boldsymbol{u}_{\rm rms}$, pure strain $\lambda_{\rm rms}$, and pure shear $s_{h\ \rm rms}$ for the three mixing sequences CF, TW, and BV.

	$\boldsymbol{u}_{\rm rms}$ (mm/s)	$\lambda_{\rm rms}$ (1/s)	$s_{h\ \rm rms}$ (1/s)
CF	3.69	0.11	0.24
TW	3.78	0.1	0.22
BV	4.42	0.1	0.22

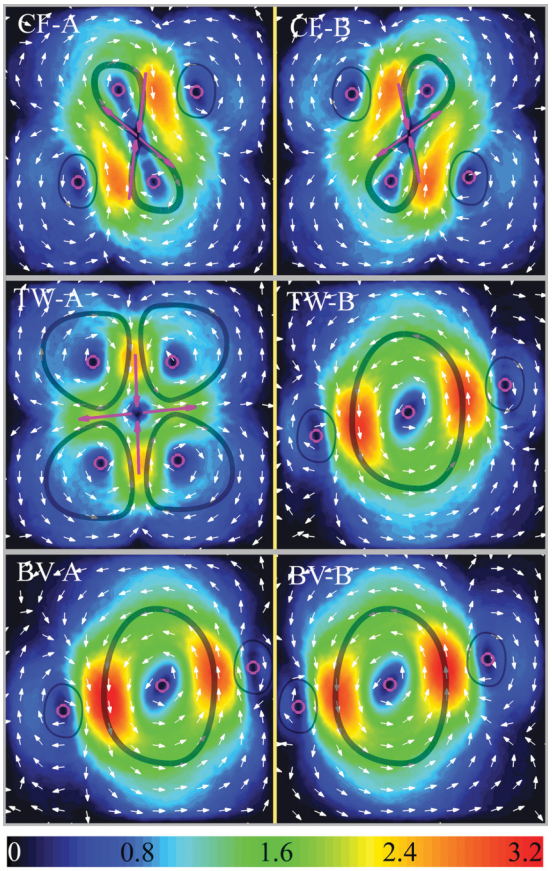

FIG. 4. (Color online) The three rows show the velocity fields during the quasisteady flow stages (denoted as A and B) of the three sequences, from top to bottom: cat's eyes flip, tendril and whorl, and blinking vortex. See also, the forcing distributions given in Fig. 3. The color map gives the spatial distribution of $\|\boldsymbol{u}\|/\boldsymbol{u}_{\text{ref}}$. The white arrows indicate the local direction of the velocity. Only one arrow is plotted for 256 measurement points. The circles indicate the centers of the eddies (elliptical stagnation points), and the arrows indicate the main direction of the central hyperbolic stagnation points. Shaded shapes are superimposed on the velocity fields to illustrate the different flow geometries.

positions of elliptical stagnation points. The main directions of stretching are indicated by arrows in the vicinity of the central hyperbolic stagnation points. The different directions of the arrows highlight that, within these hyperbolic regions, the flow is compressed in one direction and is stretched in the other direction.

Although, the viscous diffusion's time leads to a transient about $T_{\text{cyc}}/3$, the flow geometries are persistent during most of the duration of the mixing cycles. This persistence is confirmed by the temporal correlations of the velocity fields with the reference velocity fields A and B obtained during the steady stages. Figure 6 gives the maximum of these correlations, i.e., $\max\{\text{cor}[\boldsymbol{U}(t),\boldsymbol{U}_A],\text{cor}[\boldsymbol{U}(t),\boldsymbol{U}_B]\}$ with the correlation between velocity fields $\boldsymbol{U}_1$ and $\boldsymbol{U}_2$ defined as

$$\text{cor}(\boldsymbol{U}_1,\boldsymbol{U}_2) = \frac{\sum \boldsymbol{u}_1 \cdot \boldsymbol{u}_2}{N \boldsymbol{u}_{2\,\text{rms}} \boldsymbol{u}_{1\,\text{rms}}},$$

where $\boldsymbol{u}_1$, $\boldsymbol{u}_2$, $\boldsymbol{u}_{2\,\text{rms}}$, $\boldsymbol{u}_{1\,\text{rms}}$ are the N velocity vectors and the rms values of the velocity fields $\boldsymbol{U}_1$ and $\boldsymbol{U}_2$. These correlation values are higher than 0.9 during 80%, 83%, and 91% of the mixing cycles, respectively, for CF, TW, and BV sequences. Moreover, the maxima correlation values obtained are higher than 0.99 for the three sequences, whereas, the minima values are about 0.1, 0.04, and 0.36, respectively, for CF, TW, and BV sequences. As a consequence, the geometries of the flows illustrated in Fig. 4 are characteristic of the flow geometries during most of the mixing sequences.

Then, the three mixing sequences rely on combinations of flows with persisting geometries. It is interesting to briefly quantify the stretching properties of these persisting flows while details about lamination within steady flows with akin forcing and geometries can be found in Refs. [37,46]. The local stretching of flows includes terms leading to exponential and linear variations in the material element's length. They are called "pure strain" and "pure shear," respectively. To identify these two components of stretching, we use geometrical transformations of the velocity's Jacobian $\boldsymbol{J}$ defined as $\boldsymbol{J}_{ij} = \partial \boldsymbol{u}_i/\partial x_j$. The first transformation writes the Jacobian in a new orthonormal frame of reference where the first direction is an eigenvector and the second direction is orthogonal to the first direction,

$$\boldsymbol{J}' = \boldsymbol{R}_E^{-1} \boldsymbol{J} R_E = \begin{bmatrix} \lambda & b \\ 0 & -\lambda \end{bmatrix} = \begin{bmatrix} \lambda & 0 \\ 0 & -\lambda \end{bmatrix} + \begin{bmatrix} 0 & b \\ 0 & 0 \end{bmatrix}.$$

When $\det \boldsymbol{J} < 0$, λ is a real number, and the flow region is hyperbolic. In this case, the pure strain component is $|\lambda|$, and the pure shear component is $s_h = |b|$, which is also $\|\nabla \times \boldsymbol{u}\|$. It can be noticed that the pure strain form (first matrix in the split of $\boldsymbol{J}'$) is stretching in one direction and is compressing in the other with equal intensities due to the mass conservation in incompressible 2D flows. In Fig. 4, these two directions are illustrated in the vicinity of the hyperbolic stagnation points using arrows.

When $\det \boldsymbol{J} > 0$, λ is an imaginary number, and the flow region is elliptic. A second transformation is required to get

$$\boldsymbol{J}'' = \boldsymbol{R} \boldsymbol{J}' \boldsymbol{R}^{-1} = \begin{bmatrix} 0 & -KG \\ KG & 0 \end{bmatrix} + \begin{bmatrix} 0 & G(1+K) \\ 0 & 0 \end{bmatrix}.$$

In this case, the pure shear component within the elliptical domains is defined as $s_h = |G(1+K)|$, which is also $|b|$ by construction. It can be noted that there is no pure strain component within the elliptical domains. The first matrix, in the splitting of $\boldsymbol{J}''$, corresponds to a solid rotation. The reader may refer to Refs. [81–83] for further considerations about geometrical properties in 2D and 3D flows.

Table I gives the rms values λ_{rms} and $s_{h\,\text{rms}}$ for the three sequences. Using T_{flow} as the time reference, the mean dimensionless values are about 1 for pure strain and 2.3 for pure shear. Although the values obtained are higher for the shear than the strain, the exponential nature of the pure strain form is expected to make a significant contribution to the stretching.

Figure 5 complements the illustration of the persisting flows given in Fig. 4. Figure 5 shows the dimensionless distribution of pure strain (first row) and pure shear (second row) for three selected flows: CF-B, TW-A, and TW-B. The highest values of pure strain are observed in the vicinity of the central hyperbolic stagnation points with intensities typically four times higher than the rms values. Moreover, black (zero) values in the

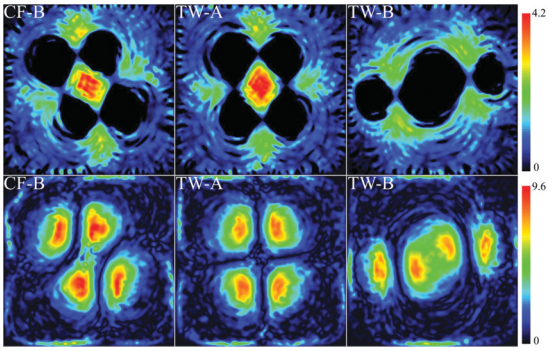

FIG. 5. (Color online) Distribution of dimensionless pure strain λ^* (first row) and pure shear s_h^* (second row) for three selected flows: CF-B, TW-A, and TW-B. The values of pure strain are set to zero within the elliptical domains, which then appear as black areas in the first row. The reference time is T_{flow}.

distribution of pure strain indicate elliptical regions and main recirculations. The presence of high values of shear within these recirculations produces a differential velocity amenable to laminate the flow [37,43,46].

Based on Figs. 4 and 5, the three flow sequences can be described before introducing their mixing and lamination properties.

The tendril and whorl sequence (second row in Fig. 4) varies the flow topology between configurations TW-A and TW-B. TW-A has a central high strain hyperbolic region surrounding a hyperbolic stagnation point, which is cornered by four recirculations. TW-B possesses a main central recirculation with two smaller recirculations on its side.

The blinking vortex sequence (third row in Fig. 4) switches between two flows (BV-A and BV-B) where the main recirculation has been translated. The flows BV-A and BV-B are similar to TW-B with different positions of eddies and small variations in the velocity maxima. In contrast with the tendril and whorl sequence, the blinking vortex sequence conserves the flow topology and does not present a central hyperbolic region with high strain. Also, it can be noted that the duration required to switch between BV-A and BV-B is small compared to the viscous and flow turnover times. Nevertheless, this duration is

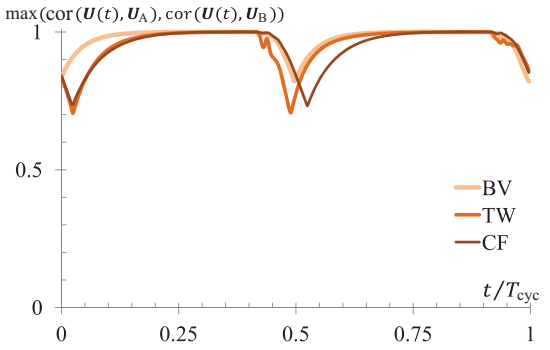

FIG. 6. (Color online) Maximum of correlations between the velocity fields at time t/T_{cyc} and the steady velocity fields (denoted as A and B) for CF, TW, and BV sequences. $\max\{\text{cor}[\boldsymbol{U}(t),\boldsymbol{U}_A],\text{cor}[\boldsymbol{U}(t),\boldsymbol{U}_B]\}$ are plotted over one period constructed using phase averaging of the PIV data.

not null, and so the blinking vortex sequence is not, strictly speaking, blinking.

The cat's eyes flip sequence (first row in Fig. 4) cyclically changes the flow between configurations CF-A and CF-B. These two flows have streamlines with inclined shapes of 8, i.e., cat's eyes, which are highlighted by shaded shapes superimposed on the velocity field. Moreover, two secondary recirculations are indicated on the sides of the 8. The cat's eyes flip sequence combines the properties of the tendril and whorl and blinking vortex sequences. It varies the geometry of the flow by changing the positions of the elliptical stagnation points and introduces a hyperbolic region (with high strain) to further stretch the flow. Some differences and novelties of the cat's eyes flip can be highlighted. First, the high strain (hyperbolic) region persists during the entire mixing cycle for the cat's eyes flip sequence. Second, the principal directions have different angles in between them. In the cat's eyes flow, the central hyperbolic region is a combination of shear and pure strains, whereas, for the tendril and whorl sequence, it is closer to pure strain where the principal directions are almost orthogonal. Third, the variation in the main directions of stretching between CF-A and CF-B is a novelty of the cat's eye flip sequence.

III. MIXING AND LAMINATION

A. Mixing

The mixing properties of the three sequences are quantified using particle color methods, e.g., Refs. [4,84–87] for single- and multispecies approaches. The flow is seeded with millions of white and black numerical particles representing the distribution of two nondiffusive dyes. The particles are tracked in time (integration of $d\mathbf{x}/dt = \mathbf{u}$ where $\mathbf{x}$ is the position of the particle and $\mathbf{u}$ is its velocity) within the flow using the PIV velocity fields. The particles' velocity is extracted from the velocity fields using polynomial interpolations on the order of 2. A Runge-Kutta four (RK4) algorithm is used for the advancement in time with a constant time step ensuring that the maximum displacement of the particles between two time steps is smaller than half the PIV mesh size. The local concentration C_{black} is measured by the number of black and white particles in 3×3 pixel boxes of the 358 μm side, i.e.,$0.009L_M$,

$$C_{\text{black}} = n_{\text{black}}/(n_{\text{black}} + n_{\text{white}}),$$

where n_{black} and n_{white} are the numbers of black and white particles within the boxes. On average, there are 126 particles per box.

The size of the counting boxes defines a diffusive length scale that we can compare to Batchelor's scale $\sqrt{D/\lambda}$ [88] in the case of a diffusive dye. With a typical pure strain rate $\lambda \simeq 0.1\,\text{s}^{-1}$, an equivalent diffusivity would be $D \sim 10^{-8}\,\text{m}^2\,\text{s}^{-1}$ for a Péclet number $\text{Pe} = U_{\text{ref}}L_M/D \sim 10^4$.

Figure 7 illustrates the mixing processes of the three sequences. The reader can also refer to the Supplemental Material, which complements Fig. 7 by giving temporal animations of these mixing sequences [89]. The first, second, and third columns are showing the cat's eyes flip, the tendril and whorl, and the blinking vortex sequences, respectively. The black dye is initially distributed above the diagonal of the mixer, and the white dye is distributed below. The rows

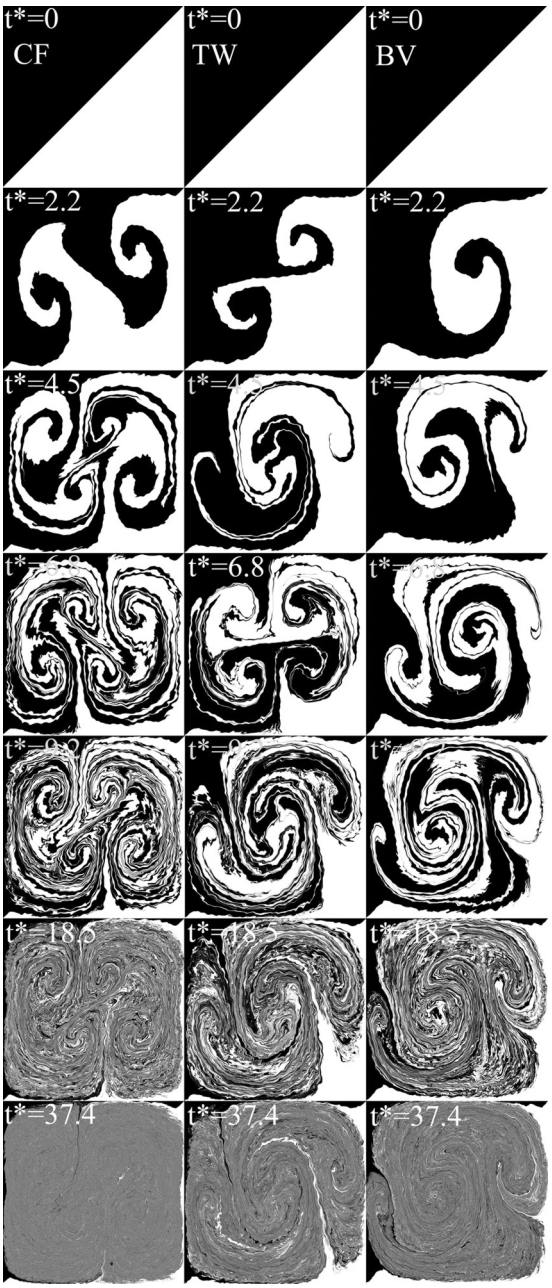

FIG. 7. The columns show the temporal evolution of the distribution of black and white numerical dyes. The three sequences are given, from left to right: CF, TW, and BV. The t^* times are: 0, 2.2, 4.5, 6.8, 9.2, 18.5, and 37.4. The time $t^* = 2.2$ corresponds to the end of the first steady forcing stage. Consecutive temporal increments are in 0.5 (until $t^* = 9.2$), 2, and 4 periods.

give the temporal advancement of the mixing. The first row shows the initial distribution of the two dyes. The second row shows the distribution of the dyes at the end of the first steady forcing stage. To highlight the different patterns regularly imposed on the dyes, Fig. 7 shows the progress of the mixing with increments of half a period during the first two periods (i.e., at times $t^* = 2.2$, 4.5, 6.8, and 9.2) before illustrating the mixing with temporal increments of two periods ($t^* = 18.5$) and four periods ($t^* = 37.4$). Each sequence can then be briefly described.

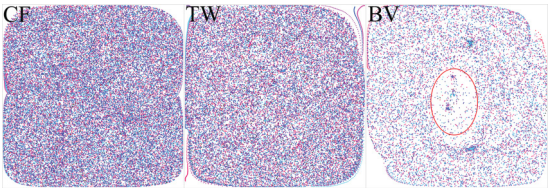

FIG. 8. (Color online) Poincaré map of the three mixing sequences CF, TW, and BV. The Poincaré maps are obtained using periodic, phase averaged velocity fields. The 22 numerical particles are tracked in time (forward and backward advancements) over 1000 periods.

For the cat's eyes flip sequence, the numerical dyes are rolled within the cat's eyes and the secondary eddies. Moreover, the dye is compressed and is stretched around the central hyperbolic stagnation point. The alternated patterns of CF-A and CF-B flows, see Fig. 4, clearly translate in alternated patterns of the dyes. After eight forcing cycles, most of the flow domain appears to be mixed.

For the tendril and whorl sequence, the numerical dyes alternatively follow the patterns imposed by the flow configurations TW-A and TW-B. During TW-A, the dyes are compressed and are stretched around the central hyperbolic stagnation point and are rolled within the four recirculations. During TW-B, the dyes are rolled within a central eddy and within two secondary eddies on its sides. It can be noticed that this central eddy is of a larger scale than the four previous recirculations.

For the blinking vortex sequence, the numerical dyes are rolled within (and around) a main eddy, which is displaced in time between two different positions. Again, the flow pattern translates to the dyes' pattern.

It is interesting to note that no islands, which often inhibit chaotic mixing [20,42], are observed for the cat's eyes flip and the tendril and whorl sequences, whereas, an island seems to be present within the heart of the central eddy for the blinking vortex sequence. Such observations are corroborated by the Poincaré maps, e.g., Refs. [49,81,90–92], illustrated in Fig. 8. The Poincaré maps of the cat's eyes flip and tendril and whorl sequences show a significant chaotic activity within the entire mixed domains, whereas, the blinking vortex sequence presents a central region with a weaker density of points. This region is highlighted by a superposed ellipse. It can be noticed that no closed orbits are found within this region. This is attributed to secondary flows, which are persistent within the heart of the translated eddy of the blinking vortex sequence. Even if these secondary flows are of weak intensity [50,51,60], they break the strict two dimensionality of the blinking vortex sequence. This dissipative feature leads to a departure from a strictly speaking Hamiltonian flow.

A first common feature of these three flow sequences is that they do not mix the corners of the mixer and some areas close to the walls. Indeed, regions close to the walls are affected by the creation of boundary layers, which act like buffers (and/or stocks of poorly mixed fluid) and reduce the mixing performance, e.g., Refs. [32,93–95]. Moving the forcing closer to the wall (and/or corners) [96] would permit two actions enhancing the uniformity of mixing within the entire mixer. First, this can flush unmixed regions towards the central region where the mixing is faster. Second, the stagnation

points resulting from the impact of jets on boundaries can be controlled and can be used to introduce sequential mixing close to the wall. It can be noticed in Figs. 4 and 7 that the three mixing sequences partially use this ability to act on the flow close to the walls. The limitation due to the corners could also be tackled by using different shapes for the boundaries of the mixer so as to suppress the corners. Such potential improvements are kept for future papers, whereas, this article focuses on the intrinsic properties of these three mixing sequences.

A second common feature is the multiplication with time of the dyes' layers inside imposed patterns. Indeed, the evolution of the dye pattern in rows 3, 5–8 reveals the reproduction of a large scale pattern with a multiplication of the number of layers, whereas, the dyes' patterns at intermediate times, e.g., row 4, are significantly different. This is in agreement with previous observations of strange eigenmodes in chaotic flows, e.g., Refs. [42,97–100]. Moreover, this growth in the number of layers is combined with a reduction in the layers' thicknesses until the dyes appear to be mixed. One novel insight explored in this article is the quantification of these layers (and the corresponding thicknesses of the striations) for the three canonical mixing sequences CF, TW, and BV.

B. Lamination

The lamination is the degree of striations of an interface. Various processes generate striations within flows, e.g., rolling and folding. The measure of lamination $\mathcal{M}_{\text{lam}}$ estimates the local degree of striations. In 2D flows, the interface is reduced to a material line. $\mathcal{M}_{\text{lam}}$ is then defined as the ratio between the total length of the line within a circle centered on the line and the diameter Φ of the circle [46],

$$\mathcal{M}_{\text{lam}} = \frac{1}{\Phi} \iint_{\text{disk}} dl.$$

Moreover, the local measure of the lamination translates into the local striations' thicknesses. This is an important point as the striations' thicknesses are the distance over which the molecular diffusion would need to act to finalize mixing in the case of diffusive dyes or species. In 2D flows, these thicknesses d are defined as

$$d = \phi/(1 + \mathcal{M}_{\text{lam}}).$$

It can be noticed that this method presents a few advantages when compared to previous methods based on the intersection of the line with prescribed sets of lines [44,45]. For example, it neither requires the definition of a set of lines or "angular corrections" nor the filtering of inappropriate orientations. Also, it does not crisscross the striations' thicknesses with "chords" [44].

To explore the lamination of the flow sequences, material lines representing the interface between two domains to be mixed are tracked in time. The line is made of interconnected virtual particles, which are tracked as described for the particle color methods with a time step used for the RK4 method two times smaller. The numerical methods used in Refs. [45,46] ensure that all particles are issuing from the initial line. In fact, due to the fast growth of the material line, this tracking method is limited as it needs to add particles between particles with an ever reducing distance, which quickly reaches the numerical accuracy of the computations. Similar to Refs. [44,101], a different method is then used. Particles are added to the line during the tracking to ensure that the distance between two consecutive particles (defining a line segment) stays small. At all times, the maximum distance between two consecutive particles is set to one tenth of the PIV mesh, i.e., $0.0024L_M$. When a line segment is longer than this maximum distance, a new particle is inserted at the center of this segment.

Figure 9 gives the temporal evolution of a material line, representing the interface of the dyes shown in Fig. 7, for the three mixing sequences: CF, TW, and BV. The reader can also refer to the Supplemental Material [89], which complements Fig. 9 by giving temporal animations of the line and its striations' thicknesses. The color scale indicates the typical thicknesses of the striations measured with $\phi = 1$ cm, i.e., $0.25L_M$. The line (and striations' thicknesses) is illustrated every half-period from $t^* = 2.2$ to $t^* = 11.6$ before the last display of the line one period later at $t^* = 16.3$. The different configurations of the stirring sequences drive the evolution of the material line. Similar to Fig. 7, regular patterns are observed, although these patterns strongly differ during a period. In addition, for the blinking vortex sequence, the displacement and temporal persistence of a potential island within the heart of the main eddy can be observed. At $t^* = 16.3$, this phenomenon leads to a lamination weaker within the heart of the eddy than for the rest of the mixed domain.

During each cycle, the folding, bending, and rolling of the line generate new striations within the flow. Indeed, the line is rolled within eddies, and it is bent close to the hyperbolic stagnation points in the direction of the unstable manifolds. Moreover, the striations' thicknesses are reduced in the direction of the stable manifolds, which enhances mixing locally, see, for example, the cat's eyes flip sequence.

For the three mixing sequences, the lamination process divides, by two or three decades, the striations' thicknesses d within 16 turnover times. As the characteristic time of diffusion decreases with d^2, the lamination significantly enhances mixing by dividing the diffusion time by ten thousands or a million in 3 minutes.

Moreover, the spatial distribution of the level of lamination (respectively, the striations' thicknesses) indicates where the mixing will first be achieved and if the mixing process is performed uniformly in space. This new insight in mixing processes can provide an interesting tool for optimizing mixers and reducing their energy consumption.

IV. DISCUSSION

It is important to characterize the nature of the processes driven by the three flow sequences in terms of stretching, lamination, and mixing. First, the stretching and lamination properties of the three flow sequences are discussed in more detail.

A. Lamination and stretching

To mix a flow, the nondiffusive stirring of the interface needs to be completed by diffusion. The distribution of the striations' thicknesses, illustrated in Fig. 9, is then key for exploring

FIG. 9. (Color) The columns show the temporal advancement of a material line for the three sequences, from left to right: CF, TW, and BV. The color scale gives the striations' thicknesses d within measurement circles of diameter $\phi = 1$ cm, illustrated (in red) at $t^* = 0$. The line tracked represents the interface between the numerical dyes in Fig. 7. Only the points for which the line's length from these points to the line's extremities is larger than $\phi/2$ are displayed.

the mixing process of a flow sequence. It is interesting to characterize a typical distance over which the diffusion would need to act to finalize the mixing within the stirred domain. To do so, we extract the spatial average of the lamination. Each measurement provides the value of the lamination at a spatial position, and the ensemble of measurements generates a cloud of values. Prior to compute the spatial average, a first local average is performed over the lamination measurements

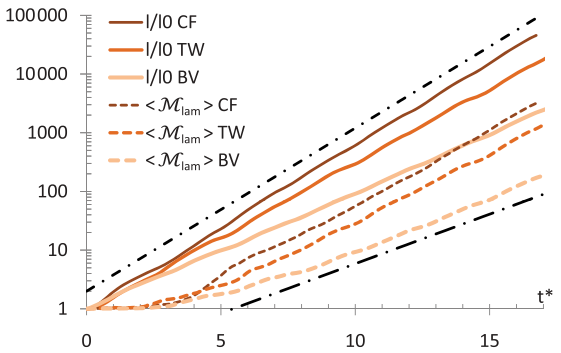

FIG. 10. (Color online) Stretching l/l_0 and spatial average of the lamination $\langle \mathcal{M}_{\text{lam}} \rangle$ versus time for the line illustrated in Fig. 9 and for the three sequences: CF, TW, and BV. $t^* = t/T_{\text{flow}}$.

contained within the elementary boxes of a regular mesh. The boxes' sides are equal to a quarter of the PIV mesh, i.e., $0.006L_M$, which is about 800 times smaller than the mixer's side. The spatial average is then performed over the boxes crossed by the line. Compared with a standard average along the line, this removes biases due to the fact that the sections of the flow with the highest lamination values also are crossed by more lines.

Similar to Refs. [45,101], the stretching of the material line is given by the line's length l divided by its initial length l_0,

$$l/l_0 = \frac{1}{l_0} \sum_i \|\mathbf{l}_i\|,$$

where $\mathbf{l}_i$ are the vectors defined by the interconnected particles.

Figure 10 gives the temporal evolution of the spatial average of the lamination, denoted as $\langle \mathcal{M}_{\text{lam}} \rangle$, for the line illustrated in Fig. 9 and the temporal evolution of the stretching of the line $\langle \mathcal{M}_{\text{lam}} \rangle$, representing the dyes' interface given in Fig. 7. Within this semilogarithmic plot, dashed-dotted lines indicate exponential trends. For the three sequences, it is striking that both $\langle \mathcal{M}_{\text{lam}} \rangle$ zand l/l_0 grow exponentially with time. Moreover, the growths observed for the three sequences are clearly different. This indicates different properties for stretching and lamination. Indeed, the cat's eyes flip sequence is found to have higher rates of lamination and stretching than the tendril and whorl and blinking vortex sequences. Also, it can be noted that, for the three sequences, the stretching rate is higher than the lamination rate.

To quantify these exponential growths and their dependence on the initial distribution of the dyes, the growths are measured for eight different orientations of lines. The different lines are obtained by simple centered rotations with regular angular increments, i.e., $\pi/8$. They correspond to the interfaces of the distributions of dyes illustrated in Fig. 12.

These results confirm the exponential growths for the stretching and the lamination for the three sequences. Moreover, the dependence on the initial distribution of dyes is weak for the cat's eyes flip and tendril and whorl sequences with standard deviations about 1% for the measured exponents. The mean values and standard deviations obtained for the growths' exponents are summarized in Table II, see columns under the heading $5L_M \times 5L_M$. It can be noted that the values of the stretching exponents, estimated using the flow periodicity as

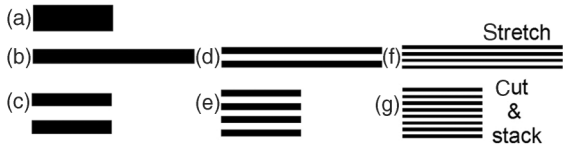

FIG. 11. Successive stretching, cutting, and stacking of material bands usually called the baker's map. The total length of the band is regularly multiplied by 2 and then grows exponentially as 2^n.

the reference of time, correspond to the topological entropy, e.g., Refs. [102,103].

It is interesting to briefly discuss the interweaving between lamination and stretching while considering lamination as a key process amenable to be engineered [37,46] rather than as a subproduct of the stretching. In this spirit, the multiplication of layers during the flow sequences enhances the stretching of the line. Indeed, if some stretching is applied within a flow region crossed by an interface, the growth of the interface is proportional to the number of layers crossing the stretched domain. The increase in the number of layers then increases the stretching. In fact, the increase in the number of layers is at the heart of the well known baker's map illustrated in Fig. 11. In this illustration, the lamination of a material band combined with a simple shear leads to an exponential growth of the material band. It can be noted that such bakerlike (exponential) growth does not need the presence of pure strain regions within the flow. Shear being present everywhere within the mixing domain, see Fig. 5, the exponential growth of the lamination is then contributing to the growth of the material line as a bakerlike process. Also, it can be noted that the increase in stretching by the lamination of interfaces is not restricted to laminar flows. Indeed, the folding of material lines has been shown to increase the line's stretching in turbulent flows [101,104].

In addition, the exponential growth of the line stretching is systematically higher than the one of the lamination with a similar increment (about 0.3) for the three sequences. Two reasons for that can be mentioned. First, the lamination is not distributed uniformly in space. Second, the pure strain present within the flows does not need lamination to generate local exponential separations of particles, e.g., Ref. [15], which leads to local exponential growths of the material lines.

Doubling the time during which the forcing stays steady allows to significantly increase the forcing period while keeping the persistence of the flows' geometries for the

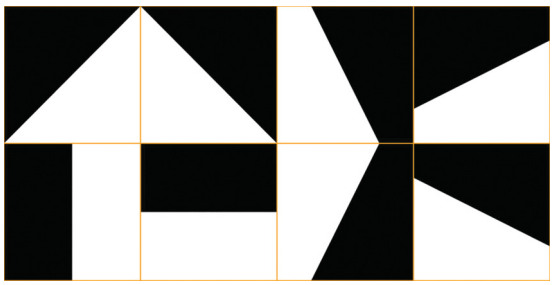

FIG. 12. (Color online) Illustration of the different initial distributions of dyes used to estimate lamination, stretching, and mixing statistics.

cat's eyes, tendril and whorl, and blinking vortex sequences. Table II gives the lamination and stretching exponents for these sequences with a period of 91.6 s, i.e., $9.1T_{\text{flow}}$. When the exponents are estimated according to the periodicity of the flows, the stretching exponents correspond to the topological entropy, e.g., Refs. [102,103]. In this case, the exponents are increasing with the increase in the period from $4.7T_{\text{flow}}$ to $9.1T_{\text{flow}}$. Moreover, it is interesting to note that the relative increase in the stretching and lamination exponents is close to the ratio of the stirring periods. Indeed, the ratios of the exponents given in Table II are about $1.85^{\pm 4.2\%}$, $1.69^{\pm 11\%}$, and $1.72^{\pm 3.2\%}$, respectively, for the CF, TW, and BV sequences, whereas, the ratio of the stirring periods is about 1.92. This indicates that, in these experiments, the characteristic flows' turnover time T_{flow} is a more consistent choice for the reference of time than the stirring period. This scaling with the flows' turnover time is attributed to the integration of the stretching and the lamination [37] during the stirring stages with persistent flow geometries.

These points suggest that the line is stretched as

$$l/l_0 \sim e^{(\lambda_{\text{ad}}+\beta_{\text{baker}})t/T_{\text{flow}}},$$

where $e^{\beta_{\text{baker}}t/T_{\text{flow}}}$ is the exponential growth of the spatial average of the lamination and $e^{\lambda_{\text{ad}}t/T_{\text{flow}}}$ represents the additional exponential stretching, which does not directly contribute to the spatial reduction in the striations' thicknesses. For these three sequences, $e^{\beta_{\text{baker}}t/T_{\text{flow}}}$ is found to be much larger than $e^{\lambda_{\text{ad}}t/T_{\text{flow}}}$.

To complement the information given by the exponential growth of the lamination, it is interesting to explore the distribution of the lamination for the three flow sequences. Figure 13 gives the probability distribution (over space) of the

TABLE II. Mean coefficients α of the exponential growths $e^{\alpha t/T_{\text{cyc}}}$, measured for the stretching l/l_0 and lamination $\langle \mathcal{M}_{\text{lam}} \rangle$ for two different sizes of mixers $5L_M \times 5L_M$ and $15L_M \times 15L_M$ and two different periods of the forcing cycle $T_{\text{cyc}} = 4.7T_{\text{flow}}$ and $T_{\text{cyc}} = 9.1T_{\text{flow}}$. The values in the superscripts give the standard deviations over different initial conditions.

		$5L_M \times 5L_M$		$15L_M \times 15L_M$	
T_{cyc}		l/l_0	$\langle \mathcal{M}_{\text{lam}} \rangle$	l/l_0	$\langle \mathcal{M}_{\text{lam}} \rangle$
$4.7T_{\text{flow}}$	CF	$3.01^{\pm 0.9\%}$	$2.71^{\pm 1.2\%}$	$2.35^{\pm 1.5\%}$	$2.00^{\pm 2.8\%}$
	TW	$2.74^{\pm 1.2\%}$	$2.42^{\pm 1.5\%}$	$2.31^{\pm 2.4\%}$	$2.03^{\pm 1.8\%}$
	BV	$2.22^{\pm 2.4\%}$	$1.91^{\pm 4.6\%}$	$1.81^{\pm 2.8\%}$	$1.51^{\pm 6.3\%}$
$9.1T_{\text{flow}}$	CF	$5.5^{\pm 1.4\%}$	$4.75^{\pm 2.7\%}$	$4.5^{\pm 3.7\%}$	$3.83^{\pm 2.3\%}$
	TW	$5.13^{\pm 2.9\%}$	$4.45^{\pm 3.3\%}$	$3.57^{\pm 3.8\%}$	$3.09^{\pm 4.4\%}$
	BV	$3.97^{\pm 1.6\%}$	$3.28^{\pm 4.9\%}$	$3.12^{\pm 3.5\%}$	$2.5^{\pm 7.4\%}$

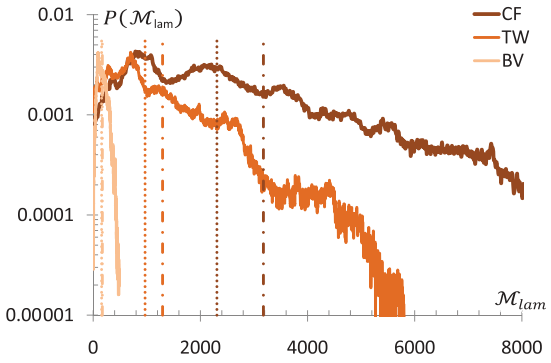

FIG. 13. (Color online) Probability distribution of the lamination for CF, TW, and BV sequences at time $t^* = 16.7$ for the line plotted in Fig. 9. Dot-dashed lines indicate the mean lamination, and dotted lines indicate the median value of the distributions.

lamination at time $t^* = 16.7$ for CF, TW, and BV sequences. Moreover, the median and average values are indicated in Fig. 13 using dot-dashed lines, respectively. The tendril and whorl and the cat's eyes flip sequences have larger tails with high local values for the lamination. This is due to the presence of the central hyperbolic region, see Fig. 4, which locally reduces the striations' thicknesses by compressing the flow in the direction of the stable manifold. The typical ratios between median and mean values are as follows: $0.75^{\pm 4.7\%}$, $0.86^{\pm 8.2\%}$, and $0.91^{\pm 5.6\%}$ for the sequences CF, TW, and BV, respectively. The superscripts indicate the standard deviations in time for $t^* > 7.3$. These ratios are consistent in time with values close to 1, whereas, the spatial average of the lamination is varying over many decades during the mixing process. This shows that the spatial average is a good estimation of the lamination occurring within these flow sequences. Moreover, the typical ratios between a reference value for which 90% of the lamination values is higher than this reference and the mean lamination are $0.22^{\pm 7.9\%}$, $0.24^{\pm 25\%}$, and $0.42^{\pm 4.8\%}$, respectively, for the sequences CF, TW, and BV. This further confirms that the spatial average of the lamination indicates the right order of magnitude for the lamination of these three sequences.

Table II also gives the exponents of the bakerlike growth measured for a larger mixing domain, i.e., $15L_M \times 15L_M$. For the three sequences, the lamination and stretching exponents measured are larger within the $5L_M \times 5L_M$ domain. The increments are about 0.7 for the cat's eyes flip sequence and about 0.4 for the tendril and whorl and the blinking vortex sequences. Indeed, when compared to the results in the larger domain, the mixing in the small domain leads every cycle to extra multiplications of the lamination and line's length by 2 for CF and 1.5 for TW and BV. From the authors' perspective, this is due to the effect of the boundaries which close the streamlines in a smaller domain. This increases the differential angular velocity [37] and reduces the turnover time at the mixer length scale. It then reinforces the lamination within the $5L_M \times 5L_M$ domain, which then, increases the stretching in a process akin to the baker's map.

B. Mixing

Figure 7 illustrates the particle color method used to measure local concentrations. To complement the picture of the stirring process (i.e., without diffusion) given by the stretching and lamination of an interface, the mixing needs to be quantified in terms of growth and homogeneity. To do so, the rescaled variance in the concentration is used to define a mixing coefficient C_{mix},

$$C_{\text{mix}} = 1 - \sigma^2/\sigma_0^2,$$

that is corrected to take into consideration the discrete sampling of the particle color method,

$$\frac{\sigma_0^2 - \sigma^2}{\sigma_0^2 - \sigma_{\text{meas}}^2} = \left(1 - \frac{\sigma^2}{\sigma_0^2}\right)\left(\frac{\sigma_0^2}{\sigma_0^2 - \sigma_{\text{meas}}^2}\right).$$

σ^2 is the variance in the dye concentration, σ_0^2 is the initial variance in the dye distribution (also maximal value of σ^2), and σ_{meas}^2 characterizes the residual variance due to the discrete sampling of the particles. Typically, σ_{meas}^2 is determined using a black and white chessboard (with cases of 1 pixel sides) for the initial distribution of the dyes before applying the stirring of the three sequences. The values obtained for σ_{meas}^2 are about $2.79\ 10^{-3}$, $2.78\ 10^{-3}$ and $3.25\ 10^{-3}$, respectively, for the CF, TW, and BV sequences. With $\sigma_0^2 = 0.25$, the corrective term $\sigma_0^2/(\sigma_0^2 - \sigma_{\text{meas}}^2)$ is about 1.01. It can be noted that this definition of a mixing coefficient is akin to quantify the relative entropy using particle color methods, e.g., Refs. [4,84].

When starting with an initial distribution of black dye covering half the mixer, the mixing coefficient has the advantage of translating into the fraction β of the mixer's domain, which has been mixed. Indeed,

$$\beta = \frac{1}{2 - C_{\text{mix}}},$$

which can be expanded as

$$\beta = C_{\text{mix}} + (1 - C_{\text{mix}})^2 - (1 - C_{\text{mix}})^3 + O(1 - C_{\text{mix}})^4.$$

When C_{mix} is close to 1, e.g., higher than 0.9, β is then close to C_{mix}. We assume that this also is true for the corrected mixing coefficient.

Figure 14 gives the corrected mixing coefficients versus time for the dye distributions of Fig. 7. After a fast growth, the mixing coefficients saturate and reach the maximum values about 0.95, 0.93, and 0.92, respectively, for CF, TW, and BV sequences. As illustrated by the gray areas of the final dyes' distribution inserted in Fig. 14, these values are in agreement with the fraction of space occupied by the domains, which have been mixed by the flow sequences.

To describe the intrinsic properties of these mixing sequences, it is important to quantify the nature of their mixing growth. The semilogarithmic inset in Fig. 14 shows an exponential decay for the concentration variance as the mixing coefficients are growing, such as $(e^{\alpha t} - 1)$ before saturation. This can be expected from the results showing an exponential growth of interfaces. Indeed, as diffusion (here, due to box counting) occurs along the interface, an exponential growth of the interfaces' length should initially lead to an exponential decay of the concentration variance.

To support this exponential behavior of the mixing produced by the three flow sequences, the mixing of a blob of dye is explored, e.g., Refs. [39,52,70,93,105,106]. The final variance σ_f^2, rescaled by its initial value at $t^* = 0$, σ_0^2, varies

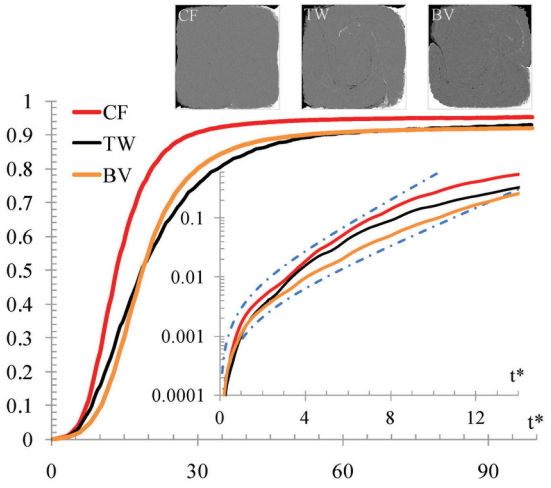

FIG. 14. (Color online) Mixing coefficient $(\sigma_0^2 - \sigma^2)/(\sigma_0^2 - \sigma_{\text{meas}}^2)$ versus time for the sequences: CF, TW, and BV. In the semilogarithmic inset, the dot-dashed lines indicate exponential growths $\sim(e^{\alpha t} - 1)$. The three picture insets at the top give the final distributions of dye for the mixing process illustrated in Fig. 7 for earlier times. From left to right, they correspond to CF, TW, and BV sequences.

according to the initial α and final β fractions of space filled by the blob of dye as

$$\frac{\sigma_f^2}{\sigma_0^2} = \left(\frac{\alpha}{1-\alpha}\right)\left(\frac{1-\beta}{\beta}\right).$$

As a consequence, the study of small blobs of dye presents the advantage to increase the variation in σ^2/σ_0^2 when the flow sequences do not mix the entire mixer's domain. For example, this ratio would be about ten times larger with $\alpha = 0.1$ than $\alpha = 0.5$.

Different blobs of dye of diameter L_M are randomly placed within the mixer and then are stirred within the flow using the particle color data. Figure 15 gives the temporal evolution of $\langle\sigma^2/\sigma_0^2\rangle$, which is the assembled average of σ^2/σ_0^2 over 24 realizations. The picture insets show the initial position of a blob of dye and the final space occupied by this mixed blob

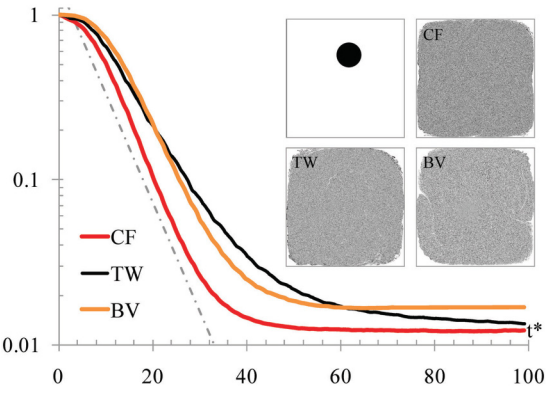

FIG. 15. (Color online) Mixing of blobs of dye. Assembled average (over 24 realizations) of concentration variance $\langle\sigma^2/\sigma_0^2\rangle$ versus time for the sequences: CF, TW, and BV. The dot-dashed line highlights an exponential trend. The picture insets illustrate the initial and final distributions for the mixing of a blob of dye.

for the three sequences. Even though the final values obtained for σ^2/σ_0^2 are significantly smaller than the ones in Fig. 14, the fractions of space occupied by the blob of dye at the end of the mixing process are similar to the ones in Fig. 14.

More importantly, the variation in $\langle\sigma^2/\sigma_0^2\rangle$, given in Fig. 15, confirms the exponential decay of the variance over more than one decade before saturation. These exponential decays contrast with previous results using moving rods to mix flows [54,93] without the need to move the walls [107,108] to enhance mixing. From the authors' perspective, this important novelty is flowing from the control of the flow's geometry using jets. Indeed, the higher values obtained for stretching and lamination in the small domain $5L_M \times 5L_M$ seem to indicate that these flow sequences are amenable for using the boundaries to reinforce the lamination and the stretching. In the present experiments, the adverse effects of the steady walls on mixing, highlighted in Ref. [93], are counterbalanced by positive effects of the walls on the flow's lamination due to the use of jets rather than rods to stir the flow.

Furthermore, to characterize the growth and robustness of the mixing, we estimate the time T_{80}^* required to reach a mixing coefficient of 80%. Similar to the stretching and lamination cases, the eight different initial distributions of dyes given in Fig. 11 are investigated. The average values measured for T_{80}^* are $21.9^{\pm 3.9\%}$, $33.8^{\pm 4.7\%}$, and $29.1^{\pm 3.1\%}$, respectively, for the cat's eyes flip, the tendril and whorl, and the blinking vortex sequences. These average values are in agreement with Fig. 14. Moreover, the small values of the standard deviations given in the superscripts indicate the robustness of the mixing sequences for different initial conditions.

C. Lamination, mixing, and saturation

The saturation of the mixing growth is an important aspect for the conception of mixers. To explore mixing saturation, the temporal derivative of the mixing coefficient, i.e., mixing rate, is investigated for the three mixing sequences.

In Fig. 16, the mixing rate is obtained by the temporal derivative of the corrected mixing coefficients given in Fig. 14. Three mixing stages can be observed in the first column of Fig. 16. The first stage corresponds to a rapid growth of the mixing rate, the second corresponds to a relative sustaining of the mixing rate, and the third corresponds to a rapid decay of the mixing rate, which then reaches relatively low values. The dotted lines plotted in the semilogarithmic graphs (right hand side column) indicate exponential trends. An exponential growth is observed for the mixing rate before the saturation of the mixing process when the mixing rate growths separate from the exponential trends. This confirms the initial exponential growth of the mixing coefficients and the exponential decay of the concentration variance. Also, in Fig. 16, it can be observed that the durations of these exponential growths differ for the three sequences.

Considering that the saturation of the mixing rate takes place when the striations' thicknesses reach the diffusive length scale of the dye (or species) to be mixed, the lamination measurements permit the estimation of the time around which the saturation of a mixing process occurs. This time depends on the diffusive properties of the dyes (or species) considered. In the case of mixing measurements using particle color

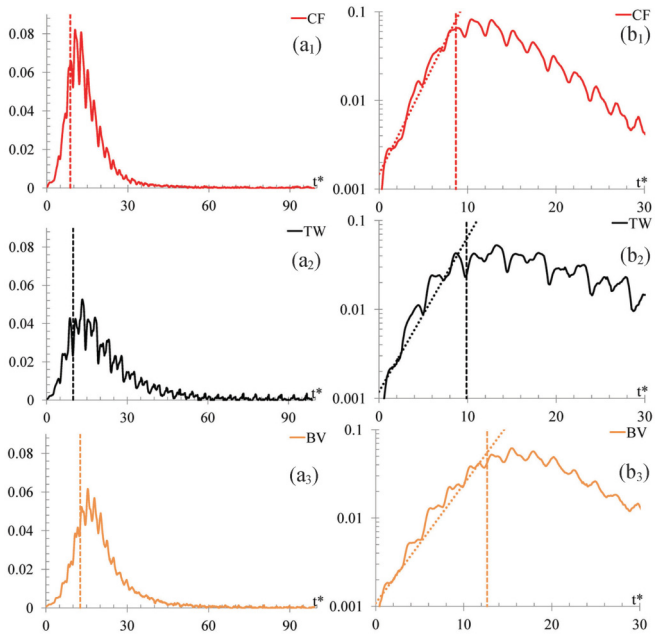

FIG. 16. (Color online) Mixing rate coefficients corresponding to the temporal derivatives of the mixing curves given in Fig. 14. The dotted lines plotted in the semilogarithmic figures [labeled (b)] show exponential trends. The dashed lines indicate the time T^*_{dif} when the spatial average of the striations' thicknesses has reached the diffusive length scale, which is given by the size of the counting box for a particle color method.

methods, this diffusive length scale is the size of the counting box. For a diffusive dye, this should be on the order of Batchelor's scale or $\sqrt{2Dt}$, whichever is the highest. The dashed lines in Fig. 16 indicate the time T^*_{dif} when the typical striations' thicknesses, estimated using the spatial average of the lamination, reach the size of the counting box. These times are 8.7, 9.9, and 12.7, respectively, for the CF, TW, and BV sequences. As observed in Fig. 16, there is good agreement between these times and the departure of the mixing rate from an exponential growth.

Given this new insight, the temporal evolution of the mixing rate can then be described as follows. For times below T^*_{dif}, the exponential stirring of the interface leads to an exponential growth of the mixing coefficient and its rate. When the striations' thicknesses reach the diffusive length scale, the diffusion swiftly finalizes the mixing process, although this process does not happen uniformly in space. While the mixing has been achieved where the typical striations' thicknesses of the interface (computed without diffusion) are below the diffusive length scale, other parts of the flow are still to be mixed. This leads to the saturation of the exponential growth of the mixing rate. Moreover, the maximum values of the mixing rate are sustained for some time after T^*_{dif}. In light of the spatial distribution of the line and its striations' thicknesses given in Fig. 9, this sustaining of the mixing rate corresponds to the sustained growth of the space filled by the interface, whereas, some parts of the flow have already been mixed. Later, when most of the space is filled by the line, the mixing rate decreases. The flow sequences are now working to ensure the homogeneity of the mixing while significant parts of the flow are already mixed.

Finally, the average thicknesses of striations can be used to estimate the range of diffusivity for which the mixing will be effective. For example, at T^*_{80}, the typical striations' thicknesses $d_{T_{80}}$, are 0.11 μm, 0.84 nm, and 0.19 μm for the CF, TW, and BV, respectively. The construction of a diffusion coefficient as $D_{80} = d^2_{T_{80}}/2T_{80}$ shows that species with diffusivity higher than 10^{-16} m^2/s will be mixed at T_{80}. For example, this includes suspensions of virus, bacteria, human cells, and DNA [14,109].

V. CONCLUSION

The control of a pair of jets driven by body forces permits the conception of tailored mixing sequences. This includes the production of sequences inspired by the tendril and whorl, blinking vortex flows, and new sequences, such as the cat's eyes flip. These sequences perform an original *in situ* mixing.

The stretching and mixing properties of these sequences have been investigated along with a new quantification of the lamination. It is shown that the lamination, the stretching, the mixing coefficient, and its rate grow exponentially in time. Comparing the exponents obtained for the exponential growth of the stretching and the lamination within two square mixing domains of different sizes (area ratio of 9) indicates that the confinement of the flow reinforces lamination and stretching. Moreover, it is shown that the lamination and stretching exponential growths are robust by doubling the duration of the steady forcing stages. This feature is attributed to the integration of the lamination (and stretching) during stirring stages with flows' geometries persisting in time. Incidentally, for the same energy or forcing input, the cat's eyes flip sequence is faster in terms of lamination, stretching, and mixing than the two other sequences.

Moreover, the estimation of the local striations' thicknesses using lamination measurements sheds new light upon mixing processes, e.g.: It shows that species with diffusivity as low as 10^{-16} m^2/s could be mixed by the three flow sequences in about 6 min, which is less than 40 turnover times. It provides the spatial distribution of the stirring process, which translates into the spatial distribution of mixing for diffusive species. It permits the estimation of the time at which the mixing rate departs from an exponential growth, leading to the saturation of the mixing process. All these new insights indicate that the exploration of the lamination should open new avenues for designing new mixers. In particular, the engineering of lamination should have an impact on mixing performances.

Finally, whereas, mixing with body forces permits the design of programmed sequences, the simplicity inherent to the control of jets should facilitate the transcription of these results to other mixing devices [3,110,111], possibly at all scales.

ACKNOWLEDGMENTS

The authors acknowledge S. Zoppellari, the Royal Society, and the EPSRC Grant No. EP/D072034/1.

[1] J. M. Ottino, Chem. Eng. Sci. **49**, 4005 (1994).
[2] V. Hessel, H. Lowe, and F. Schonfeld, Chem. Eng. Sci. **60**, 2479 (2005).
[3] F. Raynal, A. Beuf, F. Piaza, J. Scott, and P. Carriere, Phys. Fluids **19**, 017112 (2007).
[4] A. N. Cookson, D. J. Doorly, and S. J. Sherwin, Ann. Biomed. Eng. **37**, 710 (2009).
[5] P. Yager, T. Edwards, E. Fu, K. Helton, K. Nelson, M. R. Tam, and B. H. Weigl, Nature (London) **442**, 412 (2006).
[6] G. R. Helffrich and B. J. Wood, Nature (London) **412**, 501 (2001).
[7] A. Ganachaud and C. Wunsch, Nature (London) **408**, 453 (2000).
[8] L. H. Kellog, Annu. Rev. Earth Planet Sci. **20**, 365 (1992).
[9] W. I. Axford, Planet. Space Sci. **12**, 45 (1964).
[10] B. Coppi and C. Spight, Phys. Rev. Lett. **41**, 551 (1978).
[11] M. A. Avillez and M. M. Mac Low, Astrophys. J. **581**, 1047 (2002).
[12] W.-T. Kim and R. Narayan, Astrophys. J. **596**, 139 (2003).
[13] Z. Warhaft, Annu. Rev. Fluid Mech. **32**, 203 (2000).
[14] T. M. Squires and S. R. Quake, Rev. Mod. Phys. **77**, 977 (2005).
[15] L. Rossi, J. C. Vassilicos, and Y. Hardalupas, Phys. Rev. Lett. **97**, 144501 (2006).
[16] L. Rossi, J. C. Vassilicos, and Y. Hardalupas, Phys. Fluids **19**, 078108 (2007).
[17] H. Aref, J. Fluid Mech. **143**, 1 (1984).
[18] H. Aref, Phys. Fluids **14**, 1315 (2002).
[19] J. M. Ottino, Annu. Rev. Fluid Mech. **22**, 207 (1990).
[20] S. Wiggins and J. M. Ottino, Philos. Trans. R. Soc. London, Ser. A **362**, 937 (2004).
[21] O. Reynolds, *Notices of the Proceedings of the Meeting of the Members of the Royal Institution of Great Britain, London, 1893*, Vol. XIV (Royal Institution of Great Britain, London, 1893), p. 129.
[22] D. V. Khakhar, H. Rising, and J. M. Ottino, J. Fluid Mech. **172**, 419 (1986).
[23] T. H. Solomon and J. P. Gollub, Phys. Rev. A **38**, 6280 (1988).
[24] F. Raynal, F. Plaza, A. Beuf, P. Carriere, E. Souteyrand, J.-R. Martin, J.-P. Cloarec, and M. Cabrera, Phys. Fluids **16**, L63 (2004).
[25] H. Aref and S. Balachandar, Phys. Fluids **29**, 3515 (1986).
[26] J. Chaiken, C. K. Chu, M. Tabor, and Q. M. Tan, Phys. Fluids **30**, 687 (1987).
[27] T. Dombre, U. Frisch, J. M. Greene, M. Henon, A. Mehr, and A. M. Soward, J. Fluid Mech. **167**, 353 (1986).
[28] H. A. Stone, A. Nadim, and S. H. Stroatz, J. Fluid Mech. **232**, 629 (1991).
[29] T. H. Solomon, E. R. Weeks, and H. L. Swinney, Phys. Rev. Lett. **71**, 3975 (1993).
[30] C. W. Leong and J. M. Ottino, J. Fluid Mech. **209**, 463 (1989).
[31] K. Bajer and H. K. Moffatt, J. Fluid Mech. **212**, 337 (1990).
[32] F. A. Zaggout and A. D. Gilbert, Fluid Dyn. Res. **44**, 025504 (2012).
[33] G. Haller, Chaos **10**, 99 (2000).
[34] T. H. Solomon and I. Mezic, Nature (London) **425**, 376 (2003).
[35] J. L. Thiffeault, Physica D **198**, 169 (2004).
[36] J. L. Thiffeault, M. D. Finn, E. Gouillart, and T. Hall, Chaos **18**, 033123 (2008).
[37] L. Rossi, Phys. Rev. E **81**, 027301 (2010).
[38] E. Villermaux, A. D. Stroock, and H. A. Stone, Phys. Rev. E **77**, 015301 (2008).
[39] E. Villermaux and J. Duplat, Phys. Rev. Lett. **91**, 184501 (2003).
[40] R. L. Curl, AIChE J. **9**, 175 (1963).
[41] A. Venaille and J. Sommeria, Phys. Rev. Lett. **100**, 234506 (2008).
[42] J. M. Ottino, Phys. Fluids A **3**, 1417 (1991).
[43] K. Bajer, A. P. Bassom, and A. D. Gilbert, J. Fluid Mech. **437**, 395 (2001).
[44] F. J. Muzzio, P. D. Swanson, and J. M. Ottino, Phys. Fluids A **3**, 822 (1991).
[45] M. M. Alvarez, F. J. Muzzio, S. Cerbelli, A. Adrover, and M. Giona, Phys. Rev. Lett. **81**, 3395 (1998).
[46] L. Rossi and S. Lardeau, J. Turbul. **12**(6), 1 (2011).
[47] S. Ferrari and L. Rossi, Exp. Fluids **44**, 873 (2008).
[48] S. R. Quake and A. Scherer, Science **290**, 1536 (2000).
[49] R. Sturman, J. M. Ottino, and S. Wiggins, *Cambridge Monographs on Applied and Computational Mathematics* (Cambridge University Press, Cambridge, UK, 2006).
[50] L. Rossi, S. Bocquet, S. Ferrari, J. M. Garcia de la Cruz, and S. Lardeau, Int. J. Heat Fluid Flow **30**, 505 (2009).
[51] L. Rossi, J. C. Vassilicos, and Y. Hardalupas, J. Fluid Mech. **558**, 207 (2006).
[52] S. C. Jana, G. Metcalfe, and J. M. Ottino, J. Fluid Mech. **269**, 199 (1994).
[53] S. C. Jana, M. Tjahjadi, and J. M. Ottino, AIChE J. **40**, 1769 (1994).
[54] E. Gouillart, O. Dauchot, B. Dubrulle, S. Roux, and J. L. Thiffeault, Phys. Rev. E **78**, 026211 (2008).
[55] M. D. Finn and J. L. Thiffeault, SIAM Rev. **53**, 723 (2011).
[56] J. Chaiken, R. Chevray, M. Tabor, and Q. M. Tan, Proc. R. Soc. London, Ser. A **408**, 165 (1986).
[57] E. Moses and V. Steinberg, Phys. Rev. Lett. **60**, 2030 (1988).
[58] T. H. Solomon, E. R. Weeks, and H. L. Swinney, Physica D **76**, 70 (1994).
[59] R. P. Behringer, S. D. Meyers, and H. L. Swinney, Phys. Fluids A **3**, 1243 (1991).
[60] S. Lardeau, S. Ferrari, and L. Rossi, Phys. Fluids **20**, 127101 (2008).
[61] A. V. Wolf, M. G. Brown, and P. G. Prentiss, *CRC Handbook of Chemistry and Physics* (CRC, Boca Raton, FL, 1982).
[62] A. V. Wolf, *Aqueous Solutions and Body Fluids. Their Concentrative Properties and Conversion Tables* (Hoeber Medical Division, Harper & Row, New York, 1966).
[63] M. S. Paoletti and T. H. Solomon, Phys. Rev. E **72**, 046204 (2005).
[64] M. S. Paoletti and T. H. Solomon, Europhys. Lett. **69**, 819 (2005).
[65] M. E. Schwartz and T. H. Solomon, Phys. Rev. Lett. **100**, 028302 (2008).
[66] M. Raffel, C. E. Willert, and J. Kompenhans, *Particle Image Velocimetry: A Practical Guide* (Springer, Berlin, 1998).
[67] R. J. Adrian, Annu. Rev. Fluid Mech. **23**, 262 (1991).
[68] C. R. Nugent, W. M. Quarles, and T. H. Solomon, Phys. Rev. Lett. **93**, 218301 (2004).
[69] G. A. Voth, G. Haller, and J. P. Gollub, Phys. Rev. Lett. **88**, 254501 (2002).
[70] M.-C. Jullien, P. Castiglione, and P. Tabeling, Phys. Rev. Lett. **85**, 3636 (2000).
[71] S. Kenjeres, Phys. Rev. E **78**, 066309 (2008).
[72] L. Rossi and J.-P. Thibault, J. Turbul. **3**(5), 1 (2002).
[73] C. Cierpka, T. Weier, and G. Gerbeth, Phys. Fluids **22**, 075109 (2010).

[74] E. Moreau, J. Phys. D **40**, 605 (2007).
[75] *Magneto-Hydrodynamics: Historical Evolution and Trends*, edited by S. Molokov, R. Moreau, and H. K. Moffatt (Springer, Berlin, 2007).
[76] S. Cuevas, S. Smolentsev, and M. A. Abdou, Phys. Rev. E **74**, 056301 (2006).
[77] A. C. Quitry, D. H. Kelley, and N. T. Ouellette, Europhys. Lett. **94**, 64006 (2011).
[78] J.-P. Thibault and L. Rossi, J. Phys. D **36**, 2559 (2003).
[79] P. A. Davidson, *An Introduction to Magnetohydrodynamics* (Cambridge University Press, Cambridge, UK, 2001).
[80] R. A. D. Akkermans, I. P. J. Kamp, H. J. H. Clercx, and G. J. F. van Heijst, Phys. Rev. E **82**, 026314 (2010).
[81] J. M. Ottino, *The Kinematics of Mixing: Stretching, Chaos, and Transport* (Cambridge University Press, Cambridge, UK, 1989).
[82] M. S. Chong, A. E. Perry, and B. J. Cantwell, Phys. Fluids A **2**, 765 (1990).
[83] A. E. Perry and M. S. Chong, Annu. Rev. Fluid Mech. **19**, 125 (1987).
[84] J. H. Phelps and C. L. Tucker, Chem. Eng. Sci. **61**, 6826 (2006).
[85] F. R. Phelan, N. R. Hughes, and J. A. Pathak, Phys. Fluids **20**, 023101 (2008).
[86] W. Wang, I. Manas-Zloczower, and M. Kaufman, AIChE J. **49**, 1637 (2003).
[87] B. J. Binder and K. A. Landman, Phys. Rev. E **83**, 041914 (2011).
[88] G. K. Batchelor, J. Fluid Mech. **5**, 113 (1959).
[89] See Supplemental Material at http://link.aps.org/supplemental/10.1103/PhysRevE.86.026313 for the movies and animations giving the temporal illustration of mixing, stretching, and lamination for the cat's eyes flip, tendril and whorl, and blinking vortex sequences.
[90] V. N. Govorukhin, A. Morgulis, V. I. Yudovich, and G. M. Zaslavsky, Phys. Rev E **60**, 2788 (1999).
[91] R. Chabreyrie, C. Chandre, and N. Aubry, Phys. Fluids **23**, 072002 (2011).
[92] S. W. Jones, O. M. Thomas, and H. Aref, J. Fluid Mech. **209**, 335 (1989).
[93] E. Gouillart, N. Kuncio, O. Dauchot, B. Dubrulle, S. Roux, and J. L. Thiffeault, Phys. Rev. Lett. **99**, 114501 (2007).
[94] M. Chertkov and V. Lebedev, Phys. Rev. Lett. **90**, 034501 (2003).
[95] H. Salman and P. H. Haynes, Phys. Fluids **19**, 067101 (2007).
[96] L. Rossi, D. Doorly, and D. Kustrin, Europhys. Lett. **97**, 14006 (2012).
[97] D. Rothstein, E. Henry, and J. P. Gollub, Nature (London) **401**, 770 (1999).
[98] W. Liu and G. Haller, Physica D **188**, 1 (2004).
[99] E. Gouillart, O. Dauchot, J. L. Thiffeault, and S. Roux, Phys. Fluids **21**, 023603 (2009).
[100] R. T. Pierrehumbert, Chaos, Solitons Fractals **4**, 1091 (1994).
[101] S. Kida and S. Goto, Phys. Fluids **14**, 352 (2002).
[102] S. E. Newhouse, Ergod. Theory Dyn. Syst. **8**, 283 (1988).
[103] S. E. Newhouse and T. Pignataro, J. Stat. Phys. **72**, 1331 (1993).
[104] S. Goto and S. Kida, J. Fluid Mech. **586**, 59 (2007).
[105] C. Beta, K. Schneider, M. Farge, and H. Bockhorn, Chem. Eng. Sci. **58**, 1463 (2003).
[106] W. L. Chien, H. Rising, and J. M. Ottino, J. Fluid Mech. **170**, 355 (1986).
[107] E. Gouillart, J. L. Thiffeault, and O. Dauchot, Phys. Rev. Lett. **104**, 204502 (2010).
[108] J. L. Thiffeault, E. Gouillart, and O. Dauchot, Phys. Rev. E **84**, 036313 (2011).
[109] R. M. Robertson, S. Laib, and D. E. Smith, Proc. Natl. Acad. Sci. USA **103**, 7310 (2006).
[110] A. Beuf, J.-N. Gence, P. Carriere, and F. Raynal, Int. J. Heat Mass Transfer **53**, 684 (2010).
[111] H. C. Tekin, V. Sivagnanam, A. T. Ciftlik, A. Sayah, C. Vandevyver, and M. A. M. Gijs, Microfluid. Nanofluid. **10**, 749 (2011).